Amorphous Cellulose Electrolyte for Long life and Mechanically Robust Aqueous Structural Batteries

Gwendolyn J.H. Lim [a †], *J. Justin Koh* [b †], *Kwok Kiong Chan* [a], *Vivek Verma* [c], *Rodney Chua* [a], *Xue Qi Koh* [b], *Pinit Kidkhunthod* [d], *Nur Ayu Afira Sutrisnoh* [a], *Madhavi Srinivasan* [a,c,e]*

[a] School of Materials Science and Engineering, Nanyang Technological University, 50 Nanyang Ave., Singapore 639798, Singapore

[b] Institute of Materials Research and Engineering, Agency for Science, Technology and Research (A*STAR), 2 Fusionopolis Way, Innovis #08-03, 138634, Singapore

[c] Energy Research Institute at Nanyang Technological University, Research Techno Plaza, 50 Nanyang Drive, 637553, Singapore

[d] Synchrotron Light Research Institute (Public Organization), Muang, Nakhon Ratchasima, 30000, Thailand

[e] Wallenberg Initiative Materials Science for Sustainability, WISE

†These authors contributed equally

Corresponding Author: Prof. Madhavi Srinivasan
Email: madhavi@ntu.edu.sg

Abstract:

Aqueous zinc (Zn)-based structural batteries capable of both electrochemical energy storage and mechanical load-bearing capabilities are attractive for next-generation energy storage for future electric vehicles due to their eco-friendliness, non-toxic and safe nature. However, parasitic free water activities plague aqueous Zn-based batteries, detrimental to electrochemical performance and longevity of the cell. Developing polymer gel electrolytes is a notable potential solution, but they usually have poor electrode interfacial interactions and inadequate mechanical properties. This article introduces a novel non-fibrous highly amorphous cellulose polymer electrolyte "Cellyte" for aqueous structural Zn-based batteries. Cellyte exhibit high strength of ~24 MPa and Young's modulus of ~380 MPa, also with the ability to suppress parasitic water activity. The symmetric Zn||Cellyte||Zn cell therefore demonstrated excellent cycling stability of over ~3000h. Cellyte can also serve as the binder for the structural cathode material can creates a continuous polymer electrolyte–cathode interface, thereby increases mechanical robustness and decreases interfacial resistances of the battery, allowing the structural Zn||Cellyte||LMO-CF battery to achieve high electrochemical performance with excellent cycling stability over 1200h with ~91.5% capacity retention. This provides a pathway to design mechanically robust, electrochemically performing, and safe structural batteries.

Introduction:

The rise of electrical transport systems such as drones and electric vehicles (EVs) has led to the emergence of *Structural Batteries*, that are designed to possess both electrochemical energy storage and mechanical load-bearing capabilities, in hope to achieve overall mass savings or volume reduction, so as to increase system level specific energy.[1-3] Among the various batteries technologies, aqueous zinc (Zn)-based batteries have been promising candidates for next-generation energy storage devices beyond lithium-ion batteries.[4] This is due to the high theoretical capacity of metal Zn anode (820 mAh g^{-1}), low standard redox potential of Zn/Zn^{2+} (−0.76 V vs the standard hydrogen electrode (SHE), non-toxicity, eco-friendliness, low cost, and high abundance. More importantly, fabrication of aqueous Zn-based endows excellent fire safety,[5, 6] significantly enhancing safety aspects in powering future electric vehicles (EVs).

However, the major concern of aqueous Zn-based battery is the parasitic free water activities, such as uncontrolled evolution hydrogen/oxygen (HER/OER) reactions, Zn metal anode corrosion, and Zn dendrite formation , which are detrimental to the performance and longevity of the cell.[7] . To resolve the issues related to water, a possible way is to manipulate the solvation sheath of Zn^{2+} cations.[8, 9] In mild concentrations, Zn^{2+} cations are usually solvated by water in a six-fold coordination manner. Altering the coordination environment of Zn suppresses HER due to the absence of water molecules in the vicinity of Zn^{2+}, and will result in dense, non-dendritic deposition, enhancing Coulombic efficiencies and cycling stability.[5] Several techniques have been developed and most revolves around the introduction of chemical species that interacts strongly with water molecules, thereby reducing Zn-water interaction. One way is to formulate 'water-in-salt" electrolytes with sufficiently high salt concentrations, for example as 1 M $Zn(TFSI)_2$/20 M Li(TFSI) in water.[6] This would significantly reduce the water content and allow Zn^{2+} ions to be coordinated largely by the anions, and water molecules to be interacting with other species (anions and Li) apart from Zn^{2+}, (e.g. Water-TFSI complex). The other technique is molecular crowding, which involve the introduction of crowding agent (e.g. poly(ethylene glycol), poly(ethylene oxide), glucose/sucrose) to electrolytes with relatively lower salt concentration (i.e. 2 M vs 21 M LiTFSI in aqueous lithium battery). These crowding agents are capable of drawing and confining the water molecules to them through strong interactions such as hydrogen bonding, thereby reducing their activities. [10-12] Recently, polymer electrolytes have also been developed for Zn-based batteries to overcome these challenges.[5, 7, 13, 14]

Most polymer electrolytes used in aqueous Zn-based batteries are typically quasi-solid state gel-based materials due to better ionic conductivity and mechanical flexibility as compared to the sluggish kinetics provided by full solid-electrolytes.[15] Several gel electrolytes employ multiple, cross-linking additives to try to optimise absorption of water and increase mechanical strength of the electrolyte. However, these electrolytes often exhibit too much free water content, or too little water after attempts in drying out, leading to low Zn ionic conductivities.[16, 17] Even though vast improvements in Zn-based batteries have been achieved, several issues of polymer-electrolyte for Zn-based batteries remain as obstacles hindering their advancement. These issues include inadequate mechanical properties of several polymer electrolytes (mainly gels), the poor interfacial properties between the electrodes and polymer electrolyte leading to large impedance, and parasitic side reactions from failing to remove enough water.[13] Previously, Koh et al. introduced a class of materials coined as *Hydratable Plastics,* in the form of highly amorphous cellulose.[18] The key difference between such materials and hydrogels is their absorbed water content, with water being the minor component for hydratable plastics at ~45 wt% upon immersion for the highly amorphous cellulose.[18, 19] Similar to hydrogels, their polymer network is accessible to water, but the lower water content allows higher polymer interchain interactions and increases the proportion of water interacting with the polymer chains, which can be mechanically and electrochemically beneficial for polymer electrolytes. While there have been

numerous studies employing cellulose in aqueous Zn batteries, they are mainly cellulose-based separators formed through assembling fibrous cellulose (e.g. cellulose nanofibrils) into an entangled porous network.[20-22] However, porous assembly of cellulose fibers without further chemical modifications would experience tremendous mechanical decay upon contact with aqueous electrolyte solutions.[21, 23, 24] Furthermore, while they offer a sustainable alternative to commercial polyolefin-based separators, issues of electrolyte leakage and water evaporation persist, unlike solid-state polymer electrolyte.[25, 26]

In this work, highly amorphous cellulose infused with aqueous Li^{+}/Zn^{2+} electrolyte solution, hereby denoted as "Cellyte", is introduced as a polymer electrolyte for aqueous Li-Zn-hybrid structural batteries.[11, 27] Cellyte provides both electrochemical stability and mechanical robustness, therefore can be made into a multifunctional battery that demands both capabilities. With Cellyte, the symmetric Zn||Cellyte-4.5||Zn cell exhibit excellent cycling stability of over 3000h is achieved due to the efficient Zn^{2+} movement, effective suppression of zinc dendrites and parasitic reactions on the Zn anode. Using the same amorphous cellulose as binder for adhesion of the $LiMn_2O_4$ (LMO) cathode material onto the carbon fiber substrates (LMO-CF), via simple interfacial engineering, a continuous polymer electrolyte – cathode interface can be achieved when the LMO-CF structural cathode is embedded onto the surface of Cellyte, addressing the issue of poor interfacial properties between the electrode-polymer electrolyte interface. Therefore, the structural Zn||Cellyte-4.5||LMO-CF battery achieves high electrochemical performance with excellent cycling stability over 1200h with more than 91.5% capacity retention. In addition, Cellyte exhibited outstanding interfacial and mechanical properties when coupled with the LMO-CF structural cathode. The as-prepared Zn-LMO-CF structural battery is therefore highly deformation and abuse tolerant and could adapt to complex configurations without any additional mechanical support. The inherently biodegradable polymer electrolyte without any synthetic additive from fossil fuels will pave the way as a potential low-cost, sustainable, and high performance component for future structural energy storage.[28]

Results:

Material Preparation and Characterisation:

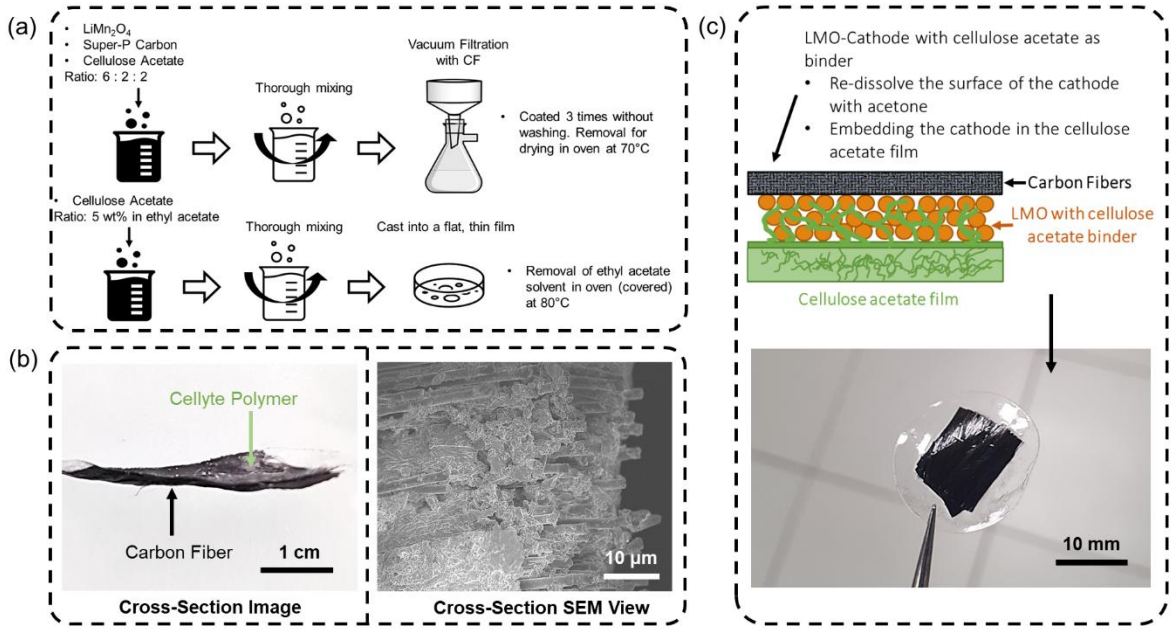


Figure 1. (a) Schematic illustration of the preparation of LMO-CF cathodes with cellulose acetate as the binder via vaccum filtration process (top). Schematic illustration of the preparation of the cellulose acetate film via casting and drying (bottom). (b) Digital image of the cross-section front view and SEM image of the cross section top view of the LMO-CF cathode embedded into cellulose film. (c) Schematic illustration and description of embedding the LMO-CF cathode into the cellulose acetate film. Digital image shows the embedded LMO-CF cathode into cellulose after hydrolysis.

The pristine amorphous cellulose film was prepared deacetylation of a cellulose acetate (CA) film (Figure 1a). For fabrication of the cellulose electrolyte (Cellyte), dried amorphous cellulose film was immersed in the following electrolyte solutions separately: 0.5m ZnTFS (Cellyte-0), 0.5m ZnTFS + 1m LiTFSI (Cellyte-1), 0.5m ZnTFS + 3m LiTFSI (Cellyte-3), and 0.5m ZnTFS + 4.5m LiTFSI (Cellyte-4.5). To prepare the LMO-CF cathodes, a homogeneous slurry solution of spinel $LiMn_2O_4$ (LMO), super-P carbon black (CB) and CA was vacuum filtrated multiple times onto de-sized uniaxial carbon fibers (Figure 1a). The ratio of the slurry solution was chosen to be 7:2:1 (LMO:CB:CA). The higher carbon black content will serve to increase electrical contact with the active LMO material, thus increasing the utilisation of active material and lowering the internal resistance of the cathode by shortening diffusion distances (Table S1, Table S1.1 and Note S1). This will therefore promote the longer cycle life of the battery.[4] The LMO-CF cathode was then subjected to the same deacetylation process to obtain the cellulose binder. To eliminate the interface between the electrolyte and the cathode, acetone was added drop-wise onto the LMO-CF cathodes before deacetylation to re-dissolve the surface of the CA binder, followed by attaching the LMO-CF cathode onto the CA electrolyte film. Upon deacetylation, a continuous transition between the LMO-CF cathode and the cellulose-electrolyte film is achieved, as illustrated in Figure 1b. After which, the LMO-CF-electrolyte composite is subjected to the same deacetlyation process to obtain a continuous amorphous cellulose matrix and interface as shown in Figure 1b. Cross-sectional digital and SEM images show that the carbon fibers, carbon black and LMO particles are well-embedded within the cellulose matrix (Figure 1c). This would reduce the electrode-electrolyte interfacial resistance, which is a common drawback of polymer electrolytes, and prevent cathode dissolution to enhance capacity retention. The image of LMO-CF embedded Cellyte prior to coin cell electrochemical characterisations is shown in Figure 1b.

Electrolyte Characterisation:

Aqueous electrolytes can be easily incorporated into the amorphous cellulose by simple immersion. This is evident by Attenuated total reflection-Fourier-transform infrared spectroscopy (ATR-FTIR) as shown in Figure 2a, where the presence of a few characteristic absorption peaks (1062, 1142, 1191, 1333 and 1357 cm^{-1}) for the Cellyte samples that correspond to the asymmetric S–N–S stretching mode of LiTFSI, C–SO_2–N bonding mode, asymmetric stretching mode of CF_3 of LiTFSI, another C–SO_2–N bonding mode of LiTFSI and the asymmetric SO_2 stretching mode of LiTFSI, respectively (Table S2 and S2.1). Indeed, these peaks related to LiTFSI are absent in both the pure hydrated cellulose sample and Cellyte-0, whereas increasing of LITFSI concentration from 1 m (Cellyte-1) to 4.5 m (Cellyte-4.5) (m = mol kg^{-1}), leads to drastic increase in the intensity these TFSI characteristic absorption peaks, suggesting a more significant incorporation of LiTFSI. On the other hand, the intensity of broad peak at 3330-3374 cm^{-1}associated to the ν(O-H) stretching vibrations (description in Table S2.1) of hydroxyl groups and water (Figure 2b), decreases with increasing ion concentration This characteristic peak can be taken as an indication of absorbed water content, with the highest in hydrated cellulose, followed by Cellyte-0, Cellyte-1, Cellyte-3 and Cellyte-4.5 in decreasing order. Beyond the 4.5 m, the 6m electrolyte solution cannot be well-incorporated into the cellulose matrix due to the reduced water content (Figure S1, Note S2). In addition, a blue-shift of this peak can also be observed with increase LiTFSI content. which can be attributed to the decrease in amount of free water molecules in the system,[29-31] which will be discuss in more detail subsequently.

The water content of hydrated cellulose, Cellyte-0 and Cellyte-4.5 is also quantitatively measured using thermogravimetric analysis (TGA, Figure 2c). The first stage of the TGA curve in Figure 2c is the dehydration process due to the removal of the volatile water component (further analysis in Note S3). It can be seen that hydrated cellulose without electrolytes incorporated contains the largest water content of 44.8 wt%, while Cellyte-0 and Cellyte-4.5 contains only around 32.5 wt% and 18.8 wt% of water, respectively. The decrease in water content can be seen in the TGA curves comparing Cellyte-0, Cellyte-1, Cellyte-3 and Cellyte-4.5 in Figure S2. Despite the lower absorbed water content, it is sufficient for cellulose chains for water molecules to percolate and form an interconnected ionically conductive network based on previous studies. [32] Apart from the water content, water also behaves behave differently in the materials. As seen from the differential scanning calorimetry measurement (DSC) in Figure 2d, the large water content of hydrated cellulose exhibits two melting peaks, one belonging to free water at around ~ 0°C similar to that of bulk water, the other belonging to freezing bound water at around ~ -16°C.[33] Similarly, Cellyte-0 exhibits both peaks, albeit at a slightly lower temperature at around ~ -3.5°C and ~ -23°C respectively, due to increased interaction with the electrolytes and the cellulose chains. In contrast, the small amount of water in Cellyte-4.5 exhibits no melting peaks at all even when cooled to -80°C, indicating significant disruption of the bulk water structure. In fact, the aqueous solution containing 0.5m ZnTFS + 4.5m LiTFSI (without cellulose polymer) shows a non-freezing behaviour up to -80°C, which suggests that the high salt concentration has already suppressed such bulk water behaviour. However, at this point it remains unclear if such disruption in bulk water structure provides an adequate molecularly crowded environment to suppress the detrimental water activities at the anode.

The stretching of O-H bond using Raman scattering spectroscopy at the spectral band of 3,000–3,800 cm^{-1}, provides insights into the bonding environment of water molecules (Figure 2e, Figure S3, Table S3). Figure 2e shows that Raman spectra of water, Cellyte-0 and Cellyte-4.5. An overall blue shift can be observed from water to Cellyte-0 to Cellyte-4.5, indicating a progressive change in the bonding environment of water with the presence of cellulose chain and increasing concentration of salt. With the deconvolution of this broad O-H peak into four peaks at around 3230, 3432, 3557 and 3630 cm^{-1},

representing tetrahedrally bonded water (3230 cm^{-1}, intermediately bonded water (3432 and 3557 cm^{-1}) and unbonded water molecules (3630 cm^{-1}) (Table S3). In general, the incorporation of cellulose chains and ions led to an overall reduction of tetrahedrally connected, "ice-like" water clusters and unbonded water, accompanied by the growth of intermediately bonded water population (Figure S3d-e, Table S3, Note S4.). Such a shift in the water bonding environment can be attributed to the reduced water content due to increased interactions with cellulose and ions, hindering water's ability to form the well-connected tetrahedrally bonded water cluster. This reduction in free water is also reflected in Cellyte-4.5 non-freezing behaviour shown in the DSC measurement (Figure 2d).

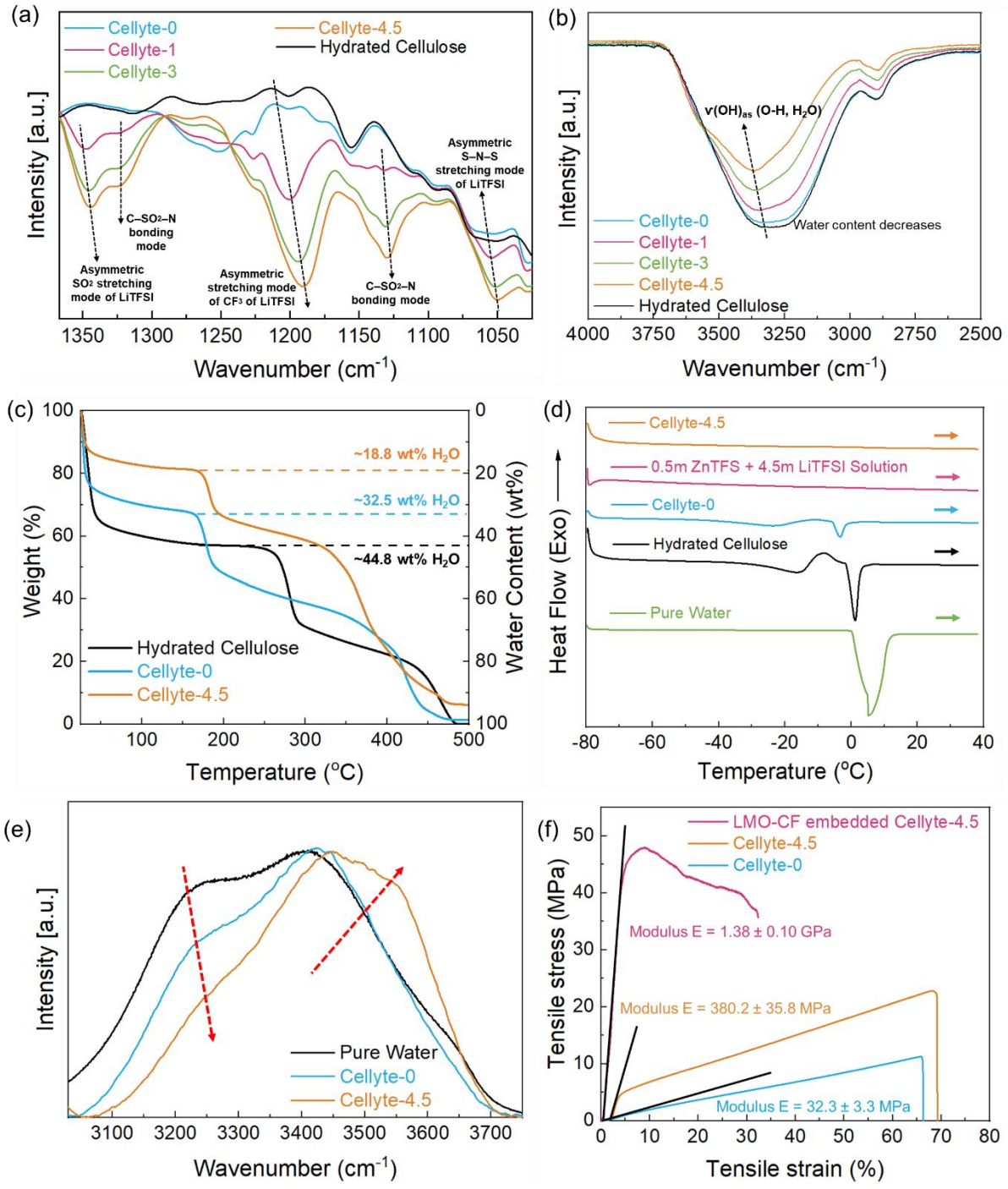


Figure 2. The evolution of the FTIR spectrum upon increasing the LiTFSI concentration. (a) The dotted display the peak positions and shift with regards to the different bonds with LiTFSI; (b) The dotted arrow signifies the

peak positions and shift with regards to water content. (c) Selected TGA analysis of the water content in Cellyte-0, Cellyte-4.5 and hydrated cellulose. (d) DSC analysis of the melting curve of the different Cellyte samples, aqueous electrolyte solution and pure hydrated cellulose. (e) Selected Raman spectra between 3,000–3,800 cm^{-1} comparing pure water, Cellyte-0 and Cellyte-4.5. (f) Stress-strain tensile plot displaying Young's Modulus (E) of LMO-CF embedded Cellyte, Cellyte-4.5 and Cellyte-0.

The ionic conductivities of hydrated cellulose, Cellyte-0 and Cellyte-4.5 were 31.1, 29.1 and 14.3 mS cm^{-1}, respectively (Electrochemical Impedance Spectroscopy (EIS), Figure S4a). The high ionic conductivity of hydrated can be attributed to the high mobility of free water in the matrix. The reduced water content in Cellyte-4.5 therefore inhibits the transfer and diffusion of water and ions alike within the crowded polymer network. Nevertheless, Cellyte-4.5 exhibits a comparable ionic conductivity to several high performing polymer electrolytes and "water-in-salt" electrolytes previously reported.[11, 27, 34] In addition, Cellyte-4.5 demonstrated a large electrochemical window, indicated by the linear voltammetry sweep (LSV, vs $Zn^{2+/}Zn$)) with a breakdown voltage of more than 2.5 V, whereas Cellyte-0 demonstrated a breakdown voltage of 2.5 V in comparison (Figure S4b). With a high breakdown voltage, this will ensure the stability of electrochemical performance at higher voltages in aqueous conditions.

The reliability of interfacial contact between the electrolyte and electrodes is one of the critical factors in determining the output performance and the mechanical stability of the aqueous structural battery. The two redox couple peaks located at 1.60/1.63 V and 1.91/1.88 V vs Zn^{2+}/Zn, correspond to the two stages of extraction and insertion of Li^+ from/into the host spinel structure of LMO into Cellyte-4.5 (Figure S5a), attributed to the oxidation and reduction of $Mn^{3+/}Mn^{4+}$ respectively. The redox couple peaks are indicated in detail in Supporting Information Note S5 and Figure S5. The appearance of these two nearly symmetrical peaks in the embedded LMO-CF in Cellyte-4.5 reveals that the Li^+ extraction/insertion in the cathodes are highly reversible (Figure S5a). On the other hand, there is only one reduction peak at 1.60 V (Figure S5b) in the CV curve for the LMO-CF cathode that was not embedded into Cellyte-4.5.This is due to the poor contact between the active cathode materials and the polymer electrolyte resulting in the large impedance, hence a large interfacial resistance in the electrode-electrolyte interface as compared to the embedded LMO-CF cathode. Even after 100 cycles at 0.5C rate, despite a slight drop in the interfacial resistance, the LMO-CF cathode that was not embedded exhibit three times larger resistance than the embedded LMO-CF cathode (Figure S5d). The values comparing the charge-transfer resistance between the cathode and electrolyte interface is displayed in Table S4. Therefore, creation of a continuous electrode-electrolyte interface through embedding the LMO-CF cathode into Cellyte enables high electrochemical performance.

Besides electrochemical performance, the embedded LMO-CF cathode also exhibits remarkable mechanical properties, which can be attributed to both the cathode and electrolyte. Cellyte-4.5 itself exhibited a tensile modulus E of 380.2 ± 35.8 MPa and a UTS of 24.2 ± 4.0 MPa, with an elongation at break of 66.4 ± 7.5% (Figure 2f). Such exceptionally high tensile modulus and UTS, makes it one of the most structurally rigid and strong hydrated polymer electrolytes as compared to convention polymer electrolytes, which are mostly gels (Table S5 for detailed comparison).[8, 16, 34-42] This can be attributed to the distinctive nature of the hydratable plastics' polymer network as compared to hydrogels. While both polymer networks are accessible to water, the lower water content in hydratable plastics allows higher polymer interchain interactions. The higher polymer interchain interactions can be expected to provide better mechanical properties, especially in terms of strength and elastic modulus, making them stronger and more rigid than gels. Therefore, despite the higher water content in Cellyte-0 leading to a larger plasticization effect, the tensile modulus E of 32.3 ± 3.3 MPa and UTS of 12.0 ± 0.7 MPa remains comfortably above typical gel electrolytes. On the other hand, the as-fabricated LMO-

CF cathode exhibited a tensile modulus E of 103.9 ± 1.3 GPa with the corresponding ultimate tensile strength (UTS) of 1.43 ± 0.1 GPa, as shown in Figure S6. This can be attributed to the remarkable mechanical properties of carbon fibers (CFs), which is an excellent reinforcement for structural cathode component as compared to other conventional battery carbon materials.[3, 4, 43] Interestingly, when the LMO-CF cathode is embedded into Cellyte-4.5, forming a structural cathode-electrolyte composite, the structural cathode-electrolyte composite exhibits a tensile modulus E of 1.38 ± 0.1 GPa with a corresponding UTS of 48 ± 1.5 MPa. By embedding the LMO-CF cathode onto Cellyte-4.5 will allow a continuous electrode-electrolyte interface without any additional fixation procedure such as tape or adhesives, providing the capability of adapting to abuse and complex mechanical deformation without largely sacrificing the electrochemical properties. The multifunctionality of the structural cathode-electrolyte is demonstrated through the mechanical load transfer onto the stiffer carbon fibers, and at the same time, reducing the interfacial resistance to enhance electrochemical performance.

Electrochemical Characterisations:

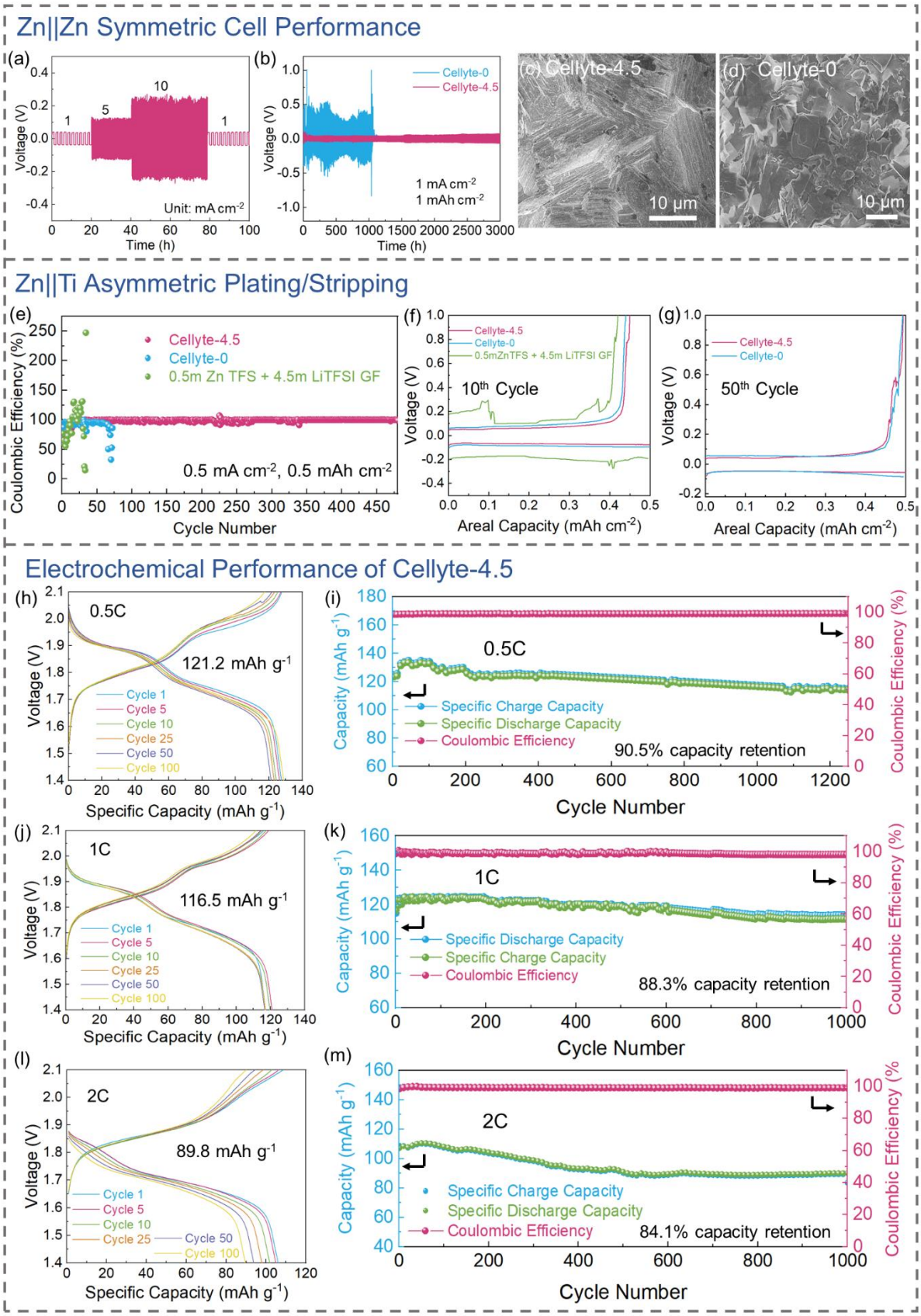


Figure 3. (a) Zn||Zn symmetric cell rate cycling performances (b) Zn||Zn symmetric cell cycling performances at 1 mA cm^{-2} and 1 mAh cm^{-2}. SEM images of the zinc foils after 100 cycles of Zn||Zn symmetric cycling using (c)

Cellyte-4.5 and (d) Cellyte-0 at the rate of 1 mA cm^{-2} and areal capacity of 1 mAh cm^{-2}. (e) Coulombic efficiencies (CE) of Zn||Ti asymmetric cells using Cellyte-4.5, Cellyte-0 and 0.5m ZnTFS + 4.5m LiTFSI soaked glass fiber (GF) at rate of 0.5 mA cm^{-2} and areal capacity of 0.5 mAh cm^{-2}. (f) The voltage profiles of Zn plating/stripping in the 10^{th} cycle and (g) 50^{th} cycle at a current density of 0.5 mA cm^{-2} and areal capacity of 0.5 mAh cm^{-2}. (h-i) Electrochemical performance of Zn||Cellyte-4.5||LMO-CF cells at 0.5C rate; (h) Charge-discharge curves of Zn||Cellyte-4.5||LMO-CF for the first 100 cycles and (i) coulombic efficiencies and cycle performances of Zn||Cellyte-4.5||LMO-CF. (j-k) Electrochemical performance of Zn||Cellyte-4.5||LMO-CF cells at 1C rate; (j) Charge-discharge curves of Zn||Cellyte-4.5||LMO-CF for the first 100 cycles and (k) coulombic efficiencies and cycle performances of Zn||Cellyte-4.5||LMO-CF. (l-m) Electrochemical performance of Zn||Cellyte-4.5||LMO-CF cells at 2C rate; (l) Charge-discharge curves of Zn||Cellyte-4.5||LMO-CF for the first 100 cycles and (m) coulombic efficiencies and cycle performances of Zn||Cellyte-4.5||LMO-CF.

Using Zn||Zn symmetric cells fabricated with Cellyte-4.5, Cellyte-0 (~108 μm thick, 19 mm wide) and glass fiber (GF) separator soaked in aqueous 0.5m ZnTFS + 4.5m LiTFSI solution (tested as control), the electrodeposition and stripping performance of Zn is shown in Figure S7 and Figure 3a-c. All cells were cycled with current density of 1 mA cm^{-2} and a capacity of 1 mAh cm^{-2}. The cell with the soaked GF separator exhibits a short cycle life (just slightly over 100 cycles, Figure S7a) and large polarisation. Zn dendrites were found piercing through the GF separator due to localisation (Figure S7b, black dots embedded in GF) and poor mechanical strength of the porous GF separator, leading to the short circuit. This is a result of excess free water activity and highly free movement of the Zn^{2+} ions, therefore Zn growth tends to localise, in this case, around the rim of the Zn foils as seen in Figure S7b. In contrast, the Zn||Zn symmetric cell containing Cellyte-4.5 displayed rather low voltage hysteresis at varied current densities as seen in Figure 3a. The enlarged profile of Zn||Zn symmetric cell containing Cellyte-4.5 at 1, 5 and 10 mA cm^{-2} (at capacity of 1 mAh cm^{-2}) is displayed in Figure S8a, S8b and S8c respectively. Even at a high current density of 10 mA cm^{-2}, overpotentials reached only around ~220mV, and revealing a highly stable plating/stripping of Zn^{2+} ions (Figure 3a and Figure S8c).

Surprisingly, it appears that Cellyte-0 and Cellyte-4.5 can both better suppress the free water activity and Zn^{2+} ion movement for a longer cycle life (> ~1000h, Figure 3b). The high mechanical strength demonstrated by the cellulose polymer itself can inhibit the fundamental perpendicular growth of the Zn, mechanically constraining the deposition within the narrow gap between the polymer surface and Zn foil, where direction of growth is limited parallelly. However, despite having similar mechanical properties, Zn||Zn symmetric cells containing Cellyte-0 ultimately has a much shorter cycle life as compared to Cellyte-4.5. The initial polarization of Cellyte-0 is ~260 mV, significantly larger than that of Cellyte-4.5, which is only ~120 mV. The polarization of Cellyte-0 continues to increase rapidly to 400 mV after 400 h and reaches an abrupt halt after ~1200 h. The detailed profile of Zn||Zn symmetric cell comparing Cellyte-0 and Cellyte-4.5 at the 80^{th} cycle, 200^{th} cycle and 1000^{th} cycle is demonstrated in Figure S9a, S9b and S9c respectively. In contrast, Cellyte-4.5 polarization remains relatively low and constant at ~40 mV throughout more than 1000 h. This difference indicates that the Zn anode interface employing Cellyte-4.5 is prominently more stable and can maintain Zn||Zn symmetric cell cycling for over 3000 hours with low polarization (Figure 3b). This is clearly demonstrated by the Zn||Zn symmetric cell containing Cellyte-4.5 with the detailed profile at the 1500^{th} cycle and 2500^{th} cycle in Figure S9d and S9e respectively. The impedance spectra of different stages of Zn||Zn symmetric cell cycling with Cellyte-4.5 was obtained at the 80^{th}, 100^{th} and 500^{th} cycle, and it confirmed that the stability of the Zn electrode does not come from "soft-short circuit" of the symmetric cell (Figure S9f-I, Note S6).[44] In addition, on opening the Zn||Zn symmetric cell containing Cellyte-4.5, there are no visible Zn dendrites embedded within Cellyte-4.5 and on the surface of the Zn foils (Figure S10a). Postmortem SEM analysis was done on the Zn foils removed from Cellyte-0 and Cellyte-4.5 Zn||Zn symmetric cells. It can be observed that more hexagonal Zn platelets were grown and orientated parallel

to the Zn electrode surface for Zn||Zn symmetric cell containing Cellyte-4.5 as seen in Figure 3c. In contrast, smaller and sharper Zn particles are formed on the Zn anode surface for the cell containing Cellyte-0 (Figure 3d). This suggests that Zn^{2+} ions are still freer to accumulate at regions of "hot-spots" of localised electric field in Cellyte-0, accelerating the perpendicular growth of Zn. These results suggest the ability of Cellyte-4.5 to reduce Zn dendrite formation much more significantly compared to Cellyte-0. Thus, excellent Zn||Zn symmetric cycling performance is achieved using Cellyte-4.5, as shown in Figure 3a. The resistance of Zn||Zn symmetric cells were further evaluated by EIS. It is clear that the Zn||Cellyte-4.5||Zn exhibit a small charge-transfer resistance, and the Zn electrode-electrolyte interface reached a stable state after extended cycling as seen by the large decrease in interfacial impedance (Figure S10b). This indicates a favourable ion-exchange and distribution of Zn^{2+} between the Zn foil interface.

To quantify the reversibility of Zn plating-stripping, Zn||Ti asymmetric cells were assembled and tested with different electrolyte conditions. At current density of 0.5 mA cm^{-2} with areal capacity of 0.5 mAh cm^{-2}, the Coulombic Efficiency (CE) of the Zn||Ti cell with aqueous electrolyte containing 0.5m ZnTFS + 4.5m LiTFSI, using a GF separator and the one with Cellyte-0 begins to have large voltage hysteresis and rapidly drops after 25 and 65 cycles, respectively, due to irreversible Zn plating/stripping. The growth of Zn dendrites due to irregular deposition on the Zn foil can penetrate the GF separator and Cellyte-0 leading to cell failure via short-circuit. In contrast, the Zn||Ti cell with Cellyte-4.5 exhibits excellent reversibility over 450 cycles (>900 h), with an average CE of 99.5% (Figure 3e). Figure 3f demonstrates the voltage profile of the 10^{th} cycle comparing the different electrolyte employed, where the CE of Cellyte-4.5 (97.8%) is the highest, followed by Cellyte-0 (95.9%) and the aqueous electrolyte-soaked GF (90.4%). At the 50^{th} cycle, both Cellyte-4.5 and Cellyte-0 exhibits similar CE and voltage profiles, but eventually the cell containing Cellyte-0 short-circuits after 70 cycles. This indicates that the parasitic side reactions can be significantly suppressed with Cellyte-4.5, and almost all the deposited Zn on the Ti mesh can be recovered during the corresponding stripping process and plated in parallel smoothly on the Zn foil. This is evident from the SEM images of the recovered Ti mesh (Figure S11c) and Zn foil using Cellyte-4.5, where it is able to guide the parallel movement of Zn^{2+} ions and result in Zn deposition along the (002) crystal plane (Figure S11a). For the cell employing Cellyte-0, rampant sharper Zn morphology can be observed in the disassembled Zn foil (Figure S11b). The smooth morphology of the Zn foil after plating/stripping will therefore extend cycle life of Zn||Ti plating/stripping with Cellyte-4.5 of over 450 cycles, preserving the high CE even at the 400^{th} cycle (Figure S11d).

The Zn||Cellyte-4.5||LMO-CF full cell performance was first evaluated in a coin cell configuration. The rate performance at 0.2C, 0.5C, 1C, 2C and 3C were determined to be 138.3, 124.5,119.6, 113.8 and 104.5 mAh g^{-1} respectively (Figure S12). The final low current cycle when returning back to 0.2C displayed similar capacities, indicating that the decrease in capacity and higher rates can be mainly attributed to the ion transport kinetics, rather than the physical degradation of cathode material or the polymer electrolyte. On further analysis on the cycling performance, at 0.5C rate, the Zn||LMO-CF full cell displayed a reversible capacity of 121.2 mAh g^{-1} after 100 cycles and demonstrated only a small 8.5% capacity decay after an outstanding 1200 cycles (Figure 3h-i). This corresponds to an excellent long cycling life of more than 3600 hours (~4.8 months). At 100 cycles, the cell containing Zn||Cellyte-4.5||LMO-CF was disassembled as seen in Figure S10c. It can be observed that the Zn foil was relatively smooth and clean without "hot-spots" and the occurrence of Zn dendrites. Dissolution of Mn from LMO was not observed and kept to a minimal as there are no observable brown residues on the cathode coin cap and Cellyte-4.5, indicating the robust nature of Cellyte-4.5 in suppressing parasitic water activity during electrochemical cycling. Post-mortem cross-sectional SEM images demonstrates that the LMO-CF remains sturdy and embedded with minimal delamination of active materials, confirming the robust

interface of LMO-CF embedded Cellyte-4.5 (Figure S10d). Energy dispersive X-ray spectroscopy (EDS) elemental mapping of Cellyte-4.5 after electrochemical cycling is further analysed for indication of Mn dissolution (Figure S13, Note S7). It is clearly observed that through the cross-sectional EDS mapping (Figure S13a) and from the top-view of the EDS mapping (Figure S13b) that there are no traces of Mn across or in the electrolyte, confirming that there is no active material dissolution even after long hours of electrochemical cycling. Following at a 1C rate, Zn||Cellyte-4.5||LMO-CF full cell displayed a reversible capacity of 116.5 mAh g^{-1} after 100 cycles with a high capacity retention rate of 90.7% after 1000 cycles (Figure 3j-k). At a higher rate of 2C, Zn||Cellyte-4.5||LMO-CF full cell displayed a significant reversible capacity of 89.8 mAh g^{-1} after 100 cycles (Figure 3l-m). Given that Cellyte-4.5 is a hydratable polymer electrolyte with limited water content and matrix-limited ion kinetics, a good capacity retention of 84.1% after 1000 cycles is achieved at a higher rate of 2C.

For comparison, LMO-CF was assembled with Zn in a coin cell containing the 0.5m ZnTFS + 4.5m LiTFSI aqueous solution soaked GF separator and a porous cellulose nanofibers (CNF) separator for full cell cycling performance (0.5C rate, Figure S14). Unlike the continuous non-fibrous Cellytes, the CNF separator is a porous mat made up of entangled nanofibers .Indeed, a large decrease and hysteresis in the specific charge/discharge capacities over 100 cycles, along with large instabilities in the cycling performance is observed for both GF and CNF fibers, as shown in in Figure S14a and S14c. After more than 200 cycles, the coin cell with the GF separator short circuits while the one with CNF separator faces a rapid capacity decay. Post-mortem analysis shows that. It can be seen clearly from Figure S14b that on the side of the GF separator facing the Zn foil, Zn dendrites was found to be embedded deep within the GF separator and localised on certain "hot-spots" on the Zn foil. In addition, the GF separator was found to be stained brown on the LMO-CF cathode side and on the cathode coin cap, which indicates the irreversible Mn dissolution from LMO during cycling. Post-mortem analysis of LMO-CF||Zn cell containing CNF separator soaked with 0.5m ZnTFS + 4.5m LiTFSI reveal that Zn dendrites are found on the Zn anode and partially piercing through the CNF separator. Slight brown stain on the cathode cap indicates the start of irreversible Mn dissolution from the LMO-CF cathode (Figure S14d). This provides two important findings. Firstly, even though the salt content of 0.5m ZnTFS + 4.5m LiTFSI creates a large disruption in the water structure (Figure S3b, Table S3), it is still insufficient to suppress parasitic water activity without the amorphous molecular cellulose network of Cellyte. Secondly, the continuous LMO-CF-Cellyte interface bounded by the cellulose matrix forms a cathode-polymer-electrolyte composite material that enhances the overall battery composite mechanical integrity, for ease of handling and crucial as a structural battery material. More importantly, the interaction between the active cathode LMO material and Cellyte is improved by the continuous cathode-electrolyte interface by minimizing Mn dissolution, improving Li^+ intercalation/de-intercalation reversibility and ultimately LMO-CF-Zn full cell electrochemical performance as observed.

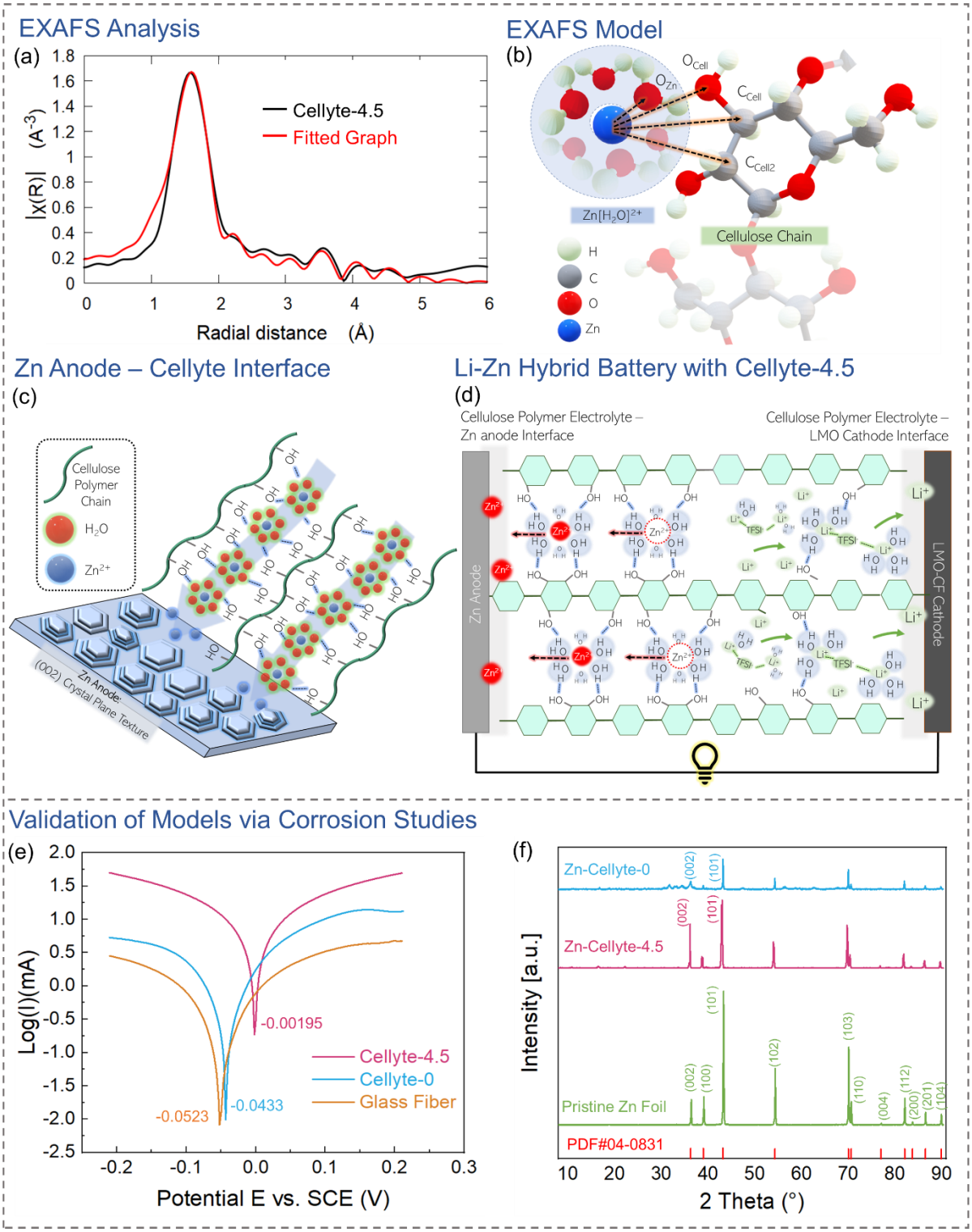


Figure 4. (a) Fourier transform EXAFS signals for Cellyte-4.5. (b) Schematics representing the Zn^{2+} coordination structure with water and cellulose in Cellyte-4.5. The colors of the sphere represent orange: Zn, dark-blue: O_{Zn}, light-blue: O_{Cell} black: C, translucent-white: H. (c) Schematic illustrating the movement and anchoring of the water molecules found in the solvated Zn^{2+} between cellulose chains. The percolation of water serves as Zn^{2+} ion conducting pathway, while the water is anchored by the cellulose polymer, preventing it from reaching the Zn anode. (d) Application of the derived model in Li-Zn hybrid battery with Cellyte-4.5 with a crowded environment for the solvated salts (Red dotted lines indicate the empty solvation shell when Zn ions move away). The electrochemical performance evaluation and characterization of Zn anodes. (e) Linear polarization curves of Zn||Zn symmetric cells with Cellyte-4.5, Cellyte-0 and aqueous electrolyte-soaked GF. (f) XRD patterns of Zn

anode at pristine state and deposited states after cycling for 100 cycles in Zn||Zn cells with Cellyte-4.5 and Cellyte-0 (0.5 mA cm^{-2}, 0.5 mAh cm^{-2}).

To understand the high reversibility of Zn plating and stripping behaviour of Cellyte-4.5, interpreting the average coordination/neighbouring environment of Zn-ions in the electrolyte is essential.[45, 46] Using (X-ray Absorption Spectroscopy) XAS, Extended X-ray Absorption Fine Structure (EXAFS) has been analysed for the Zn^{2+} ion centre in the Cellyte-4.5 system. The Fourier transform EXAFS signal for the zinc K-edge in the Zn-cellulose system is shown in Figure 4a, with fitting details in Table S6. Due to the presence of the polymer, the coordination environment around Zn^{2+} can be quantified even beyond ~3.5 Å (but < 5.5 Å) due to the steric effect in packing of the cellulose chains. In Figure 4a, the first and also the largest peak is observed and can be fitted to nearly 6 oxygen atoms coordinating Zn with a Zn−O bond distance of ~2.09 Å (Figure 4b, Table S6). The Zn-O bond distance also agrees with several modelling studies that are done.[47-50] This essentially represents that a hexa-hydrated Zn^{2+} coordination complex forms as the primary zinc shell in the electrolyte system. Unfortunately, despite the presence of cellulose chains and salt ions to interact with water, the six-fold water-coordinated solvation sheath of Zn^{2+} ions remain intact, which does not explain the extremely high electrochemical stability of Cellyte-4.5.

However, beyond the primary shell, a second highest peak is also observed roughly around ~4 Å, and the peak can be fitted with the 4 Zn-O bonds at a distance of ~4.15 Å. These O atoms can most likely be assigned to the O atoms that belong to the cellulose chain as shown in the figure, located outside the primary zinc hydration shell. The assignment of O at ~4.15 Å to cellulose is further supported by the fact that for a good fit, 4 C atoms at a distance of 4.31 A and 6 C atoms at a distance of ~4.7 Å had to be added. These multiple C atoms at farther distances would come from the cellulose backbone.[48] Lastly, the assignment of two oxygen atoms at 4.41 Å will represent the ether oxygen further away from the Zn centre, that exists along the cellulose backbone. Hence, based on the distances and the elements, this model proposes that cellulose hydroxyl groups form a second shell of Zn^{2+}, outside of Zn^{2+} primary hydration shell as seen in the illustration Figure 4b.

The conduction of Zn^{2+} can further understood from the interactions Zn^{2+}, water and cellulose. Despite the molecular crowding effect from the various ions, fully coordinated hydration shell of Zn^{2+} exist in Cellyte-4.5 as seen from EFXAS and the schematic in Figure 4b. However, peculiarly, the electrochemical stability and cycle performance of LMO-CF||Cellyte-4.5||Zn remains high, indicating that battery electrodes and cell degradation did not happen while maintaining high capacity retention. The long cycle life and good capacity output indicates impressive electrochemical stability, which can be attributed to the anchoring of the water molecules in the first shell surrounding Zn^{2+} ion (solvation sheath) by the cellulose chains that exists on the second shell away from the Zn^{2+} ion. Water molecules within cellulose are known to consist of a significant proportion that are immobilized by the hydroxyl groups of cellulose, especially at lower hydration levels.[51] The residence time of immobile water molecules in cellulose can be longer than 10 μs,[51] whereas the residence time for first hydration shell water molecules of Zn^{2+} is known to be between 100 ps and 5 ns,[47, 52] and perhaps closer to lower limit according to some studies.[53] Therefore, this immobilisation of water molecules by cellulose acting as an anchoring shell can explain the good electrochemical performance of Cellyte-4.5. Water molecules even though fully solvated around the Zn^{2+} ions, are likely unable to exit the polymer electrolyte-electrode interface due to anchoring by cellulose, therefore minimizing the parasitic water activity and side reactions that can occur on the Zn anode (Figure 4c). As such, the optimised Li-Zn hybrid battery with Cellyte-4.5 can be illustrated in the schematic Figure 4d with Zn plating/stripping on the Zn anode interface and Li^{+} intercalation/ de-intercalation in the LMO-CF cathode (during charge/discharge respectively) with the crowded water environment derived from the polymer

electrolyte characterisations. The combination of immobilisation of water molecules by cellulose acting as an anchoring shell while the optimal LiTFSI salt concentration added to confine the parasitic water molecules to minimum help significantly improve the aqueous Li-Zn structural battery performance.

The immobilisation of water molecules by the cellulose polymer chains can also be observed through the rate-limiting step of the anode zinc deposition via the activation energy (E_a) of the Arrhenius equation:

$$\frac{1}{R_{ct}} = Ae^{(-E_a/RT)}$$

Where R_{ct} is the interface resistance, A is the frequency factor, R is the gas constant and T is the absolute temperature. In aqueous liquid electrolyte, Zn ions usually exist as $[Zn(H_2O)_6]^{2+}$, therefore a large amount of energy is provided for the desolvation process when depositing at the interface of Zn foil, easily generating hydrogen evolution reactions (HER) and unwanted side reactions and by-products. If $[Zn(H_2O)_6]^{2+}$ can be desolvated in advance before reaching the Zn anode interface, side reactions and by-products will be significantly reduced. The fact that the strong polar hydroxyl groups in Cellyte can interact more strongly with and thereby anchoring the water molecules around Zn^{2+}, helps in inhibiting water from leaving the polymer electrolyte onto the Zn anode. From Figure S15a and S15b, the variable temperature EIS demonstrate that R_{ct} of Zn foil in aqueous electrolyte-soaked GF (575 Ω) is significantly larger than that in Cellyte-4.5 (52 Ω) at 303.15 K after 20 cycles, confirming the charge-transfer ability. The E_a in Cellyte-4.5 is therefore calculated to be about 17.06 kJ mol^{-1} while the E_a in the aqueous electrolyte-soaked GF is 33.41 kJ mol^{-1}, indicating anchoring of water molecules within Cellyte is highly possible.

Therefore, the corrosion behaviour of the Zn anode for Cellyte-4.5, Cellyte-0 and soaked GF in aqueous electrolyte is further evaluated by the Tafel curves obtained after prolonged Zn||Zn symmetric cell cycling (0.5 mA cm^{-2}, 0.5 mAh cm^{-2}). As demonstrated, the corrosion potential of Zn metal in Cellyte-4.5 is the highest (-0.00195 V), compared to Cellyte-0 (-0.0433 V) and aqueous electrolyte in GF (-0.0523 V) after 100 cycles (Figure 4e) . It is also noted that for Cellyte-4.5, the corrosion current is significantly reduced. Electrolytes with a higher corrosion potential has less corrosion tendency on the Zn anode, while a smaller corrosion current indicates a lower corrosion rate.[54-56] Therefore, this confirms that the parasitic side reactions with water can be effectively mediated by Cellyte-4.5. In addition, X-ray diffraction (XRD) was employed to inspect the surface of pristine Zn foil, and Zn anode surface after 100 cycles with Cellyte-4.5 and Cellyte-0 (Figure 4f). For the Zn surface employing Cellyte-4.5, no distinctive by-products were detected in the XRD pattern in comparison to Cellyte-0. More significantly, the (002)/(101) peak intensity ratio significantly increased from 0.189 to 0.791 during the 100 cycles employing Cellyte-4.5 as compared to the pristine Zn foil, signifying the growth of Zn (002) was predominant in forming a uniform and homogeneous electrodeposited Zn surface. This confirms the hypothesis of the ability of Cellyte-4.5 in anchoring the water molecules to inhibit parasitic side reactions, improving Zn-ion conduction and reversibility.

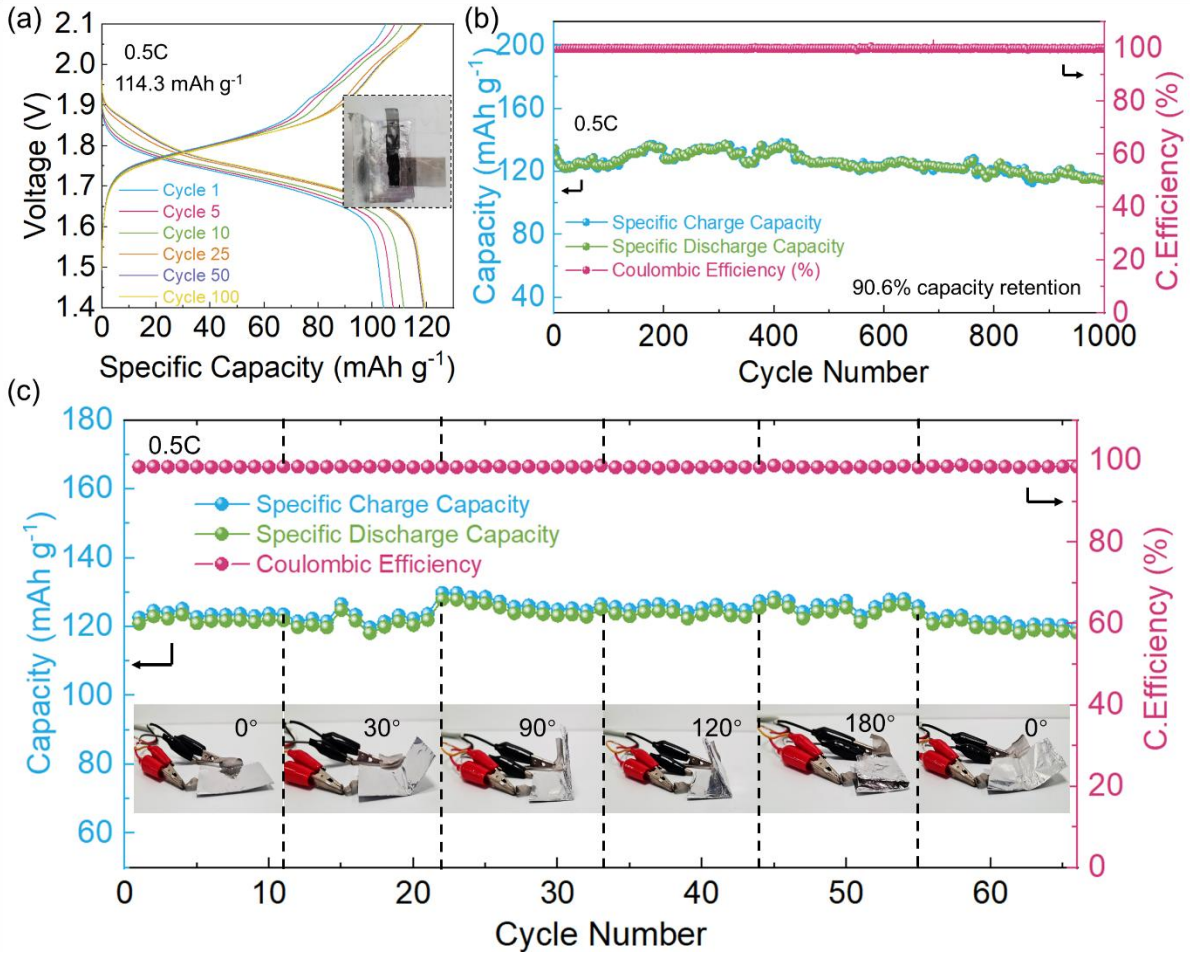


Figure 5. (a) Charge-discharge curves of Zn||Cellyte-4.5||LMO-CF pouch cell for the first 100 cycles and (b) coulombic efficiencies and cycle performances of Zn||Cellyte-4.5||LMO-CF pouch cell. Electrochemical performance under deformation: (c) Comparison of variation in charge-discharge capacities and coulombic efficiencies of Zn||Cellyte-4.5||LMO-CF pouch cell under different bending angles.

The Zn||Cellyte-4.5||LMO-CF full cell configuration is then adapted into a pouch cell (width: 5 cm x length: 8 cm, LMO-CF cathode ~2-3 cm long) to demonstrate the feasibility of fabricating larger scale structural battery pack. The inset in Figure 5a shows the image of the pouch cell fabricated. When cycled at 0.5C, the Zn||Cellyte-4.5||LMO-CF pouch cell demonstrated a high specific capacity of 126.1 mAh g^{-1} after 100 cycles. Albeit with slight variations in the charge/discharge capacities throughout the cycles, the Zn||Cellyte-4.5||LMO-CF pouch cell exhibited a long cycle life of over 1000 hours and achieved good capacity retention of 90.6% (Figure 5b). The assembled pouch cell is also determined to be highly deformation tolerant. The Zn||Cellyte-4.5||LMO-CF pouch cell was electrochemically tested at a 0.5C rate under several bending conditions, with angles ranging from 0° to 180°. It can be observed that at any given bending angle, the charge-discharge specific capacity performances are within highly tolerable range. The specific discharge capacity of the pouch cell at a 0°, 30°, 90°, 120°, 180° and 0°(recovery) are obtained to be at 119.4, 122.9, 122.4, 123.2 and 121.1 mAh g^{-1} respectively, while the Coulombic Efficiency is highly stable at an average of 98.6%. The corresponding photographs of the pouch cells are displayed in Figure 5c, demonstrating the behaviour under different bending conditions. The stability of the of the voltage and charge-discharge polarisation curves can be seen in the individual charge-discharge curves demonstrated in Figure S16. These results confirmed that there is stable ion transport and power output even under deformation stress and recovery conditions due to the mechanical robustness of the Zn||LMO-CF structural battery composite.

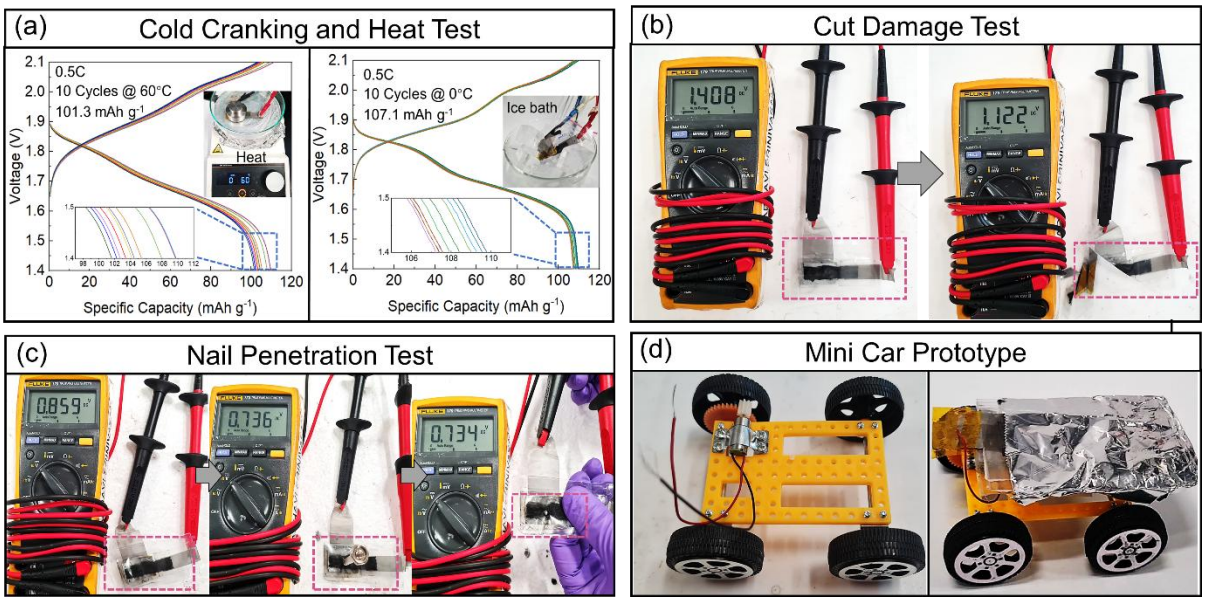


Figure 6. Environmental adaptation and durability tests: (a) Environmental adaptive tests: heating of Zn||Cellyte-4.5||LMO-CF pouch cell at 60°C and its corresponding charge-discharge curves cycled at 0.5C rate for 10 cycles. A separate pouch cell was placed in an ice-bath for sub-zero condition simulation, with the corresponding discharge curves for 10 cycles. (b) Damage by cutting and exposing the pouch cell while retaining its open-circuit voltage (OCV). (c) Damage of pouch cell by nail penetration while retaining OCV. (d) Application of Concept in Prototype: Fabrication of Zn||Cellyte-4.5||LMO-CF structural pouch cells for toy car prototype.

Varying range of ambient thermal conditions, along with their resilience and durability when subjected to mechanical forces are also important for multifunctional structural batteries in practical applications. When the Zn||Cellyte-4.5||LMO-CF pouch cell is subjected to higher temperature heating (60°C under compression, Figure 6a), it can obtain an impressive discharge capacity of 101.3 mAh g^{-1} after 10 cycles at 0.5C rate, indicating high heat resilience. In contrast, when the Zn||Cellyte-4.5||LMO-CF pouch cell is submerged into an ice bath (Figure 6a), the specific discharge capacity is very well maintained for over 10 cycles at 107.2 mAh g^{-1} at 0.5C rate, indicating superb performance under sub-zero conditions. When further subjected to physical abuse, the electrochemical reliability of the Zn||Cellyte-4.5||LMO-CF pouch cell during the deformation is remarkable. The Zn||Cellyte-4.5||LMO-CF pouch cell was cut out into several pieces (Video S1, Figure 6b), while still holding the voltage. When an identical pouch cell was subjected to a nail penetration test, the voltage was held even after puncture (Figure 6c). In addition, when the punctured Zn||Cellyte-4.5||LMO-CF pouch cell was subjected to galvanostatic charge and discharge at 0.5C rate, the stability of the specific discharge capacity was retained at 121.8 mAh g^{-1} as seen in Figure S17b. Lastly, when the Zn||Cellyte-4.5||LMO-CF pouch cell cover was cut and removed, the internal components were exposed to air and ambient conditions with around 50% humidity as seen in Figure S18a. The cell can maintain a specific discharge capacity of 110.3 mAh g^{-1} for 20 cycles (around 30 hours, Figure S18c). Evaporation tests at 40% relative humidity (RH) has shown the ability of Cellyte-4.5 to retain a 95.9% electrolyte weight (~4% water mass loss), and maintain a 102.7% electrolyte weight at 70% RH (Figure S18b). The ability of Cellyte-4.5 to scavenge water from the environment increases its resilience against electrolyte leakage and drying in the case of damage. Such adaptability and durability of the Zn||Cellyte-4.5||LMO-CF structural battery is crucial for safety for applications in mobile ground or aerial vehicles.

To demonstrate its potential as structural battery for transport devices, the Zn||Cellyte-4.5||LMO-CF pouch cell is incorporated as a structural battery for a mini prototype toy car. The mini toy car prototype was solely powered by two laminated pouch cells with dimensions of 4.0 cm × 5.0 cm × 0.6 mm (L ×

$W \times T$). With the laminated cells (Figure 6d), the mini prototype car can move smoothly, which can also attributed to the stiffness and light-weight nature of the Zn||Cellyte-4.5||LMO-CF structural batteries (Video S2). The lightness and smaller volume of the batteries are essential in realisation for structural energy storage in lightweighting aerial and potentially electric vehicles.

Conclusion:

In summary, a new class of aqueous polymer electrolyte, *Hydratable Plastics,* in the form of highly amorphous cellulose, is introduced as mechanically robust and tough solid electrolytes for aqueous structural batteries. Cellulose-based electrolytes (Cellyte) is not only eco-friendly and biodegradable, but also highly processable in an ambient environment. From the Zn-hybrid aqueous battery perspective, Cellyte mitigates problems faced in aqueous electrolytes through manipulating the water molecules' behaviour around Zn^{2+}. This helps to i) reduce water activity and water decomposition during stripping/plating at the Zn anode and ii) effective suppress of Zn dendrites. The symmetric Zn||Cellyte-4.5||Zn cell therefore demonstrated excellent cycling stability of over 3000h. From a structural battery point-of-view, a continuous Cellyte polymer-cathode interface achieved when the LMO-CF structural cathode is embedded onto the surface of Cellyte. This will address the issue of poor interfacial properties between the electrode and polymer electrolyte, increase mechanical integrity and prevent capacity fade due to cathode material dissolution. Therefore, the structural Zn||Cellyte-4.5||LMO-CF battery achieves high electrochemical performance with excellent cycling stability over 1200h with more than 91.5% capacity retention. The structural battery is demonstrated to be highly environmentally adaptive, deformation tolerant and abuse resistant. The adaptability and sustainability of the designs allows potential for future low-cost energy storage designs, which will serve as a guideline for developing safe electric vehicles with high mass savings.

Methods:

Materials:

Super-P carbon black (conductive, 99+% metals basis, Alfa Aesar), $LiMn_2O_4$ (Merck), Dimethyl Sulfoxide (DMSO, ACS reagent, ⩾ 99.9%, Sigma-Aldrich), Zinc (Zn) metal foil (Goodfellow), cellulose Acetate (CA, average Mn ~50,000 by GPC, Sigma-Aldrich), ethyl acetate (ACS reagent, ⩾ 99.5%, Merk) uniaxial carbon fibers (Hexcel AS4C 12K filament) were used without further purification. Lithium bis(trifluoromethanesulfonyl)imide (LiTFSI, 99.95% trace metals basis, Sigma-Aldrich) and zinc trifluoromethanesulfonate (ZnTFS, 98%, Sigma-Aldrich) salts are used in preparing the electrolyte without further purification. Methanol (MeOH, ACS reagent, ⩾99.8%, Sigma-Aldrich) and sodium hydroxide (NaOH reagent grade, ⩾98%, pellets (anhydrous), Merck) are used in preparing the hydrolysis solution for CA without further purification. Whatman glass microfiber filter papers were used as separators.

Preparation of Cellulose-based Polymer Electrolyte (Cellyte):

Cellulose acetate (CA, 1.0 g) was fully dissolved in ethyl acetate (21 mL). The pristine amorphous cellulose film was prepared casting the solution of CA dissolved in ethyl acetate into a glass petri dish then drying overnight in an oven at 60°C. The CA film is removed and subjected to deacetalyation in an alkaline solution (1 wt% NaOH in MeOH) for 3 hours to obtain the regenerated amorphous cellulose film. The hydrated cellulose film was rinsed thoroughly several times in DI water, until the pH of the water reaches 6.5. The film was kept in DI water until use. The hydrated polymer film has a thickness of ~114 – 120 μm.

For fabrication of the cellulose electrolyte (Cellyte), the hydrated cellulose film was dried fully in a vacuum oven at 70°C for 24 hours, before immersing the films in the corresponding electrolyte solutions

separately: 0.5m ZnTFS (Cellyte-0), 0.5m ZnTFS + 1m LiTFSI (Cellyte-1), 0.5m ZnTFS + 3m LiTFSI (Cellyte-3), and 0.5m ZnTFS + 4.5m LiTFSI (Cellyte-4.5), where m = mol kg^{-1}. The films will remain immersed in the aqueous electrolyte solution for more than 24 hours until use.

Preparation of the LMO-Carbon Fiber Cathode:

The uniaxial carbon fibers was de-sized in acetone, and washed thoroughly in DI water. The carbon fibers are dried fully in a oven at 80°C until use. A homogeneous slurry solution of spinel $LiMn_2O_4$ (LMO), super-P carbon black and CA in the ratio of 7:2:1 was dissolved fully in DMSO and stirred for 3 days. The slurry was vacuum filtrated 3 times onto de-sized uniaxial carbon fibers and dried fully in a vacuum oven at 70°C for 24 hours. The mass loading of LMO obtained per cm^2 of carbon fiber sample is ~4.3 - 4.6 mg. The LMO-CF cathode was then subjected to the same hydrolysis process to obtain the regeneration of the cellulose binder.

Preparation of the embedded LMO-Carbon Fiber Cellyte:

50 μL of acetone was added drop-wise onto per 1 cm^2 of LMO-CF cathodes before hydrolysis to re-dissolve the surface of the CA binder, followed by attaching the LMO-CF cathode onto the CA film and drying completely, before subjecting to hydrolysis. The embedded LMO-Carbon Fiber Cellulose was then immersed into 0.5m ZnTFS + 4.5m LiTFSI aqueous electrolyte for more than 24 hours before use.

Physical Characterization of self-standing LMO and LMO-sandwiched CF cathodes:

The morphologies of the LMO-CF cathode and dried polymer materials were characterized using the scanning electron microscope (SEM, Jeol FE6340F, 5kV).

The thermal degradation behaviour of Cellyte-X (X = 0, 1, 3 and 4.5) were analysed through thermogravimetric analysis (TGA) using the TGA Q500 (TA Instruments). The samples were heated from 30 °C to 800 °C at the heating rate of 3 °C/min in O_2/N_2 at a flow rate of 40 mL/min and 60 mL/min, respectively.

Differential Scanning Calorimetry: DSC Q100 Calorimeter (TA Instruments) was used to test for the DSC data. The samples were initially equilibrated at 25 °C, then cooled to –80 °C at a 3 °C min^{-1} rate. Then, the samples were heated to 40 °C at a 3 °C min^{-1} rate. Empty pans were used as the reference sample.

Mechanical Tests:

LMO-Carbon Fiber Cathode: Tensile tests were performed on Instron 5569 Table Universal testing machine in ambient room temperature conditions. Three strip samples with widths of 10 mm and a nominal gauge length of 20 mm were used for the tensile tests with a rate of 5 mm per minute under a 100 kN load. The strength values obtained are the stress and strain at break.

Cellyte Samples and Embedded LMO-Carbon Fiber Cellyte: Tensile tests were performed on Instron 5569 Table Universal testing machine in ambient room temperature conditions. Three strip samples with widths of 10 mm and a nominal gauge length of 30 mm were used for the tensile tests with a rate of 5 mm per minute under a 10 kN load. The strength values obtained are the stress and strain at break. The samples are all soaked in aqueous electrolytes (in wet state) before measurements.

Electrochemical Characterizations of the aqueous polymer electrolyte and system:

Ionic Conductivity: CR2016 type coin cells using two SS as blocking electrodes (SS/Cellyte-X/SS) were used for the measurements (X = 0, 1, 3 and 4.5). The ionic conductivities of the polymer electrolyte were measured by AC electrochemical impedance spectroscopy (EIS) using the Biologic SP-300 battery

tester with a frequency range from 10^{-2} to 10^{6} Hz with a signal amplitude of 10 mV. The ionic conductivity (σ) of the electrolytes was then calculated by the R_b value as follows:

$$\sigma = \frac{L}{R_b A}$$

where L and A are the thickness and effective area of the polymer electrolyte, respectively.

Interfacial impedance was determined by EIS for the LMO-CF cathode (embedded in Cellyte-4.5 and non-embedded) as the working electrode, and Zn foil as the counter electrode using the Biologic SP-300 battery tester with a frequency range from 10^{-2} to 10^{6} Hz with a signal amplitude of 10 mV.

Cycling voltammetry (CV) tests were carried out in a coin-cell configuration (CR2016 type coin cells) with the LMO-CF cathode (embedded in Cellyte-4.5 and non-embedded) as the working electrode, and Zn foil as the counter electrode using the Biologic SP-300 battery tester at scan rates of 0.5 mV s^{-1} and 1 mV s^{-1}.

To determine the electrochemical stability window of the polymer electrolyte, the linear sweep voltammetry technique (BioLogic SP-300 battery tester) is applied on the coin cell assembled with Ti and Zn foil as the positive and counter electrode, respectively, together with Cellyte-X (X = 0, 1, 3 and 4.5)

The hydrogen bonding behaviour of the electrolyte mixtures was probed using confocal Raman (excimer laser wavelength 532 nm, Renishaw InVia). For the Raman measurements conducted on the various electrolytes with a laser power of 50%, a total of 2 accumulations with an integration time of 10 s per accumulation is acquired for each sample spectra.

2.4 Electrochemical Characterization of Aqueous Polymer Electrolyte Batteries:

Coin cell preparation for Zn//Zn symmetrical cells: Soaked Cellyte-4.5 was cut into discs with a 19 mm radius. Zn metal foil was cut into discs with a 12 mm radius, and was used as both the electrodes. For the counter supporting experiment, Whatman glass microfiber filter paper was used as the separator and 4.5m LiTFSI + 0.5m ZnTFS in DI water was used as the aqueous electrolyte. 12 mm radius Zn metal foil discs was used as both the electrodes. Separate coin cells (CR2016) were then assembled in room temperature ambient conditions.

Coin cell preparation of LMO-CF cathode (non-embedded): The cathodes were prepared using carbon fibers that are 1 cm (L) by 1 cm (W). Soaked Cellyte-4.5 was cut into 19 mm radius disc and 12 mm Zn metal foil disc was used as the counter electrode. For the counter supporting experiment, 12 mm Zn metal foil disc was used as the counter electrode, the Whatman glass microfiber filter paper was used as the separator, and the hybrid aqueous Li-Zn ions electrolyte (4.5 m LiTFSI + 0.5 m ZnTFS) was used. Separate coin cells (CR2016) were then assembled in room temperature ambient conditions.

Coin cell preparation of LMO-CF cathode (embedded): The cathodes (1 cm by 1cm) were first embedded into Cellyte-4.5 before the LMO-CF embedded Cellyte-4.5 was cut into 19 mm discs. 12 mm Zn metal foil disc was used as the counter electrode and coin cells (CR2016) were then assembled in room temperature ambient conditions.

Pouch cell preparation: The LMO-CF cathodes were prepared into 3 cm (L) by 1 cm (W) dimensions before embedded into Cellyte-4.5 (prepared into a dimension of 3.5cm (L) by 2.5 cm (W)). The LMO-CF embedded Cellyte-4.5 was soaked for at least 2 days to fully soak the aqueous electrolyte solution. The Zn metal foil was cut into a 3 cm (L) by 1 cm (W) dimension. A laminating pouch was used for the pouch cell casing and was cut and laminated according to the size of the battery required.

Battery testing: Galvanostatic charge and discharge (GCD) measurements were investigated and analysed using the Neware BTS system for both the assembled coin cells and pouch cells. The cells are cycled between the voltage of 2.1 V and 1.4 V with various current densities.

Acknowledgement

The authors acknowledge the grant from A*STAR under the Advanced Manufacturing and Engineering (AME) programmatic fund number A20H3b0140. This project is also partially supported by RIE2025 MTC Young Individual Research Grant (Grant no. M22K3c0101), administered by Agency of Science, Technology and Research (A*STAR). The authors also acknowledge the support from Wallenberg Initiative Materials Science for Sustainability, WISE.

Declaration of interests

The authors declare no conflict of interest.

Author Contributions

G.J.H Lim and J.J. Koh contributed equally to this work.

Supporting Information

The following is the Supporting Information to this article:

References:

[1] L.E. Asp, E.S. Greenhalgh, Structural power composites, Composites science and technology 101 (2014) 41-61.

[2] L.E. Asp, M. Johansson, G. Lindbergh, J. Xu, D. Zenkert, Structural battery composites: a review, Functional Composites and Structures 1(4) (2019) 042001.

[3] D. Safanama, S.W. Chien, K. Jenssen, M.Y. Tan, N. Ding, D.W.H. Fam, Fibre-reinforced multifunctional composite solid electrolytes for structural batteries, Composites Science and Technology (2023) 110134.

[4] G.J.H. Lim, R. Chua, J.J. Koh, K.K. Chan, E.J.J. Tang, V. Teh, M. Srinivasan, Structural and conformable designs for aqueous multifunctional batteries, Materials Today Energy 33 (2023) 101255.

[5] J. Shin, J. Lee, Y. Park, J.W. Choi, Aqueous zinc ion batteries: focus on zinc metal anodes, Chemical science 11(8) (2020) 2028-2044.

[6] F. Wang, O. Borodin, T. Gao, X. Fan, W. Sun, F. Han, A. Faraone, J.A. Dura, K. Xu, C. Wang, Highly reversible zinc metal anode for aqueous batteries, Nature materials 17(6) (2018) 543-549.

[7] J. Fu, Z.P. Cano, M.G. Park, A. Yu, M. Fowler, Z. Chen, Electrically rechargeable zinc–air batteries: progress, challenges, and perspectives, Advanced materials 29(7) (2017) 1604685.

[8] P. Sun, W. Liu, D. Yang, Y. Zhang, W. Xiong, S. Li, J. Chen, J. Tian, L. Zhang, Stable Zn anodes enabled by high-modulus agarose gel electrolyte with confined water molecule mobility, Electrochimica Acta 429 (2022) 140985.

[9] H. Lu, S. Zheng, L. Wei, X. Zhang, X. Guo, Manipulating Zn2+ solvation environment in poly (propylene glycol)-based aqueous Li+/Zn2+ electrolytes for high-voltage hybrid ion batteries, Carbon Energy (2023) e365.

[10] J. Xie, Z. Liang, Y.-C. Lu, Molecular crowding electrolytes for high-voltage aqueous batteries, Nature materials 19(9) (2020) 1006-1011.

[11] D.E. Ciurduc, C. de la Cruz, N. Patil, A. Mavrandonakis, R. Marcilla, Molecular crowding bi-salt electrolyte for aqueous zinc hybrid batteries, Energy Storage Materials 53 (2022) 532-543.

[12] L. Suo, O. Borodin, T. Gao, M. Olguin, J. Ho, X. Fan, C. Luo, C. Wang, K. Xu, "Water-in-salt" electrolyte enables high-voltage aqueous lithium-ion chemistries, Science 350(6263) (2015) 938-943.

[13] K. Wu, J. Huang, J. Yi, X. Liu, Y. Liu, Y. Wang, J. Zhang, Y. Xia, Recent advances in polymer electrolytes for zinc ion batteries: mechanisms, properties, and perspectives, Advanced Energy Materials 10(12) (2020) 1903977.

[14] W. Yang, Y. Yang, H. Yang, H. Zhou, Regulating water activity for rechargeable zinc-ion batteries: Progress and perspective, ACS Energy Letters 7(8) (2022) 2515-2530.

[15] G. Yuqi, G. Lim, V. Verma, C. Yi, R. Chua, N. Lim, M. Srinivasan, Solid State Zinc and Aluminum ion batteries: Challenges and Opportunities, ChemSusChem (2023) e202202297.

[16] L. Xu, T. Meng, X. Zheng, T. Li, A.H. Brozena, Y. Mao, Q. Zhang, B.C. Clifford, J. Rao, L. Hu, Nanocellulose-Carboxymethylcellulose Electrolyte for Stable, High-Rate Zinc-Ion Batteries, Advanced Functional Materials (2023) 2302098.

[17] M. Muddasar, A. Beaucamp, M. Culebras, M.N. Collins, Cellulose: Characteristics and applications for rechargeable batteries, International Journal of Biological Macromolecules (2022).

[18] J.J. Koh, G.J.H. Lim, S. Chakraborty, Y. Zhang, S. Liu, X. Zhang, S.C. Tan, Z. Lyu, J. Ding, C. He, Robust, 3D-printed hydratable plastics for effective solar desalination, Nano Energy 79 (2021) 105436.

[19] J.J. Koh, P. Pang, S. Chakraborty, J. Kong, A. Sng, P. Anukunwithaya, S. Huang, X.Q. Koh, C. Thenarianto, W. Thitsartan, Presence, origins and effect of stable surface hydration on regenerated cellulose for underwater oil-repellent membranes, Journal of Colloid and Interface Science 635 (2023) 197-207.

[20] Y. Zhang, Z. Liu, X. Li, L. Fan, Y. Shuai, N. Zhang, Loosening Zinc Ions from Separator Boosts Stable Zn Plating/Striping Behavior for Aqueous Zinc Ion Batteries, Advanced Energy Materials 13(42) (2023) 2302126.

[21] S. Yang, Y. Zhang, Y. Zhang, J. Deng, N. Chen, S. Xie, Y. Ma, Z. Wang, Designing Anti-Swelling Nanocellulose Separators with Stable and Fast Ion Transport Channels for Efficient Aqueous Zinc-Ion Batteries, Advanced Functional Materials (2023) 2304280.

[22] Z. Zheng, S. Guo, M. Yan, Y. Luo, F. Cao, A Functional Janus Ag Nanowires/Bacterial Cellulose Separator for High-Performance Dendrite-Free Zinc Anode Under Harsh Conditions, Advanced Materials 35(47) (2023) 2304667.

[23] J. Wang, W. Chen, T. Dong, H. Wang, S. Si, X. Li, Enabled cellulose nanopaper with outstanding water stability and wet strength via activated residual lignin as a reinforcement, Green Chemistry 23(24) (2021) 10062-10070.

[24] A.J. Benítez, J. Torres-Rendon, M. Poutanen, A. Walther, Humidity and multiscale structure govern mechanical properties and deformation modes in films of native cellulose nanofibrils, Biomacromolecules 14(12) (2013) 4497-4506.

[25] W. Wang, C. Li, S. Liu, J. Zhang, D. Zhang, J. Du, Q. Zhang, Y. Yao, Flexible Quasi-Solid-State Aqueous Zinc-Ion Batteries: Design Principles, Functionalization Strategies, and Applications, Advanced Energy Materials 13(18) (2023) 2300250.

[26] H. Dong, J. Li, J. Guo, F. Lai, F. Zhao, Y. Jiao, D.J.L. Brett, T. Liu, G. He, I.P. Parkin, Insights on flexible zinc-ion batteries from lab research to commercialization, Advanced Materials 33(20) (2021) 2007548.

[27] C. Yan, Y. Wang, Z. Chen, X. Deng, Hygroscopic Double-Layer Gel Polymer Electrolyte toward High-Performance Low-Temperature Zinc Hybrid Batteries, Batteries & Supercaps 4(10) (2021) 1627-1635.

[28] Y. Ye, L. Yu, E. Lizundia, Y. Zhu, C. Chen, F. Jiang, Cellulose-Based Ionic Conductor: An Emerging Material toward Sustainable Devices, Chemical Reviews 123(15) (2023) 9204-9264.

[29] X. Liu, Z. Yu, E. Sarnello, K. Qian, S. Seifert, R.E. Winans, L. Cheng, T. Li, Microscopic understanding of the ionic networks of “water-in-salt” electrolytes, Energy Material Advances (2021).

[30] B. Auer, R. Kumar, J.R. Schmidt, J.L. Skinner, Hydrogen bonding and Raman, IR, and 2D-IR spectroscopy of dilute HOD in liquid D2O, Proceedings of the National Academy of Sciences 104(36) (2007) 14215-14220.

[31] J. Lim, K. Park, H. Lee, J. Kim, K. Kwak, M. Cho, Nanometric water channels in water-in-salt lithium ion battery electrolyte, Journal of the American Chemical Society 140(46) (2018) 15661-15667.

[32] K. Kulasinski, S. Keten, S.V. Churakov, R. Guyer, J. Carmeliet, D. Derome, Molecular mechanism of moisture-induced transition in amorphous cellulose, ACS Macro Letters 3(10) (2014) 1037-1040.

[33] H. Hatakeyama, T. Hatakeyama, Interaction between water and hydrophilic polymers, Thermochimica acta 308(1-2) (1998) 3-22.

[34] Y. Yan, S. Duan, B. Liu, S. Wu, Y. Alsaid, B. Yao, S. Nandi, Y. Du, T.W. Wang, Y. Li, Tough Hydrogel Electrolytes for Anti-Freezing Zinc-Ion Batteries, Advanced Materials 35(18) (2023) 2211673.

[35] P. Lin, J. Cong, J. Li, M. Zhang, P. Lai, J. Zeng, Y. Yang, J. Zhao, Achieving ultra-long lifespan Zn metal anodes by manipulating desolvation effect and Zn deposition orientation in a multiple cross-linked hydrogel electrolyte, Energy Storage Materials 49 (2022) 172-180.

[36] M. Chen, J. Chen, W. Zhou, X. Han, Y. Yao, C.P. Wong, Realizing an all-round hydrogel electrolyte toward environmentally adaptive dendrite-free aqueous Zn–MnO2 batteries, Advanced Materials 33(9) (2021) 2007559.

[37] N. Zhao, F. Wu, Y. Xing, W. Qu, N. Chen, Y. Shang, M. Yan, Y. Li, L. Li, R. Chen, Flexible hydrogel electrolyte with superior mechanical properties based on poly (vinyl alcohol) and bacterial cellulose for the solid-state zinc–air batteries, ACS applied materials & interfaces 11(17) (2019) 15537-15542.

[38] L. Li, L. Zhang, W. Guo, C. Chang, J. Wang, Z. Cong, X. Pu, High-performance dual-ion Zn batteries enabled by a polyzwitterionic hydrogel electrolyte with regulated anion/cation transport and suppressed Zn dendrite growth, Journal of Materials Chemistry A 9(43) (2021) 24325-24335.

[39] W. Xu, C. Liu, Q. Wu, W. Xie, W.-Y. Kim, S.-Y. Lee, J. Gwon, A stretchable solid-state zinc ion battery based on a cellulose nanofiber–polyacrylamide hydrogel electrolyte and a Mg 0.23 V 2 O 5· 1.0 H 2 O cathode, Journal of Materials Chemistry A 8(35) (2020) 18327-18337.

[40] F. Mo, Z. Chen, G. Liang, D. Wang, Y. Zhao, H. Li, B. Dong, C. Zhi, Zwitterionic sulfobetaine hydrogel electrolyte building separated positive/negative ion migration channels for aqueous Zn-MnO2 batteries with superior rate capabilities, Advanced Energy Materials 10(16) (2020) 2000035.

[41] Y. Quan, M. Chen, W. Zhou, Q. Tian, J. Chen, High-performance anti-freezing flexible Zn-MnO2 battery based on polyacrylamide/graphene oxide/ethylene glycol gel electrolyte, Frontiers in Chemistry 8 (2020) 603.

[42] Z. Liu, D. Wang, Z. Tang, G. Liang, Q. Yang, H. Li, L. Ma, F. Mo, C. Zhi, A mechanically durable and device-level tough Zn-MnO2 battery with high flexibility, Energy Storage Materials 23 (2019) 636-645.

[43] N.A.A. Sutrisnoh, G.J.H. Lim, K.K. Chan, J.J.N. Lim, M. Srinivasan, Structural cathodes: Navigating the challenges in fabrication and multifunctional performance analysis, Composites Science and Technology (2023) 110147.

[44] Q. Li, A. Chen, D. Wang, Z. Pei, C. Zhi, “Soft shorts” hidden in zinc metal anode research, Joule 6(2) (2022) 273-279.

[45] G. Zhang, Y. Chen, L. Fu, L. Zheng, K. Fan, C. Zhang, J. Zou, H. Dai, L. Guan, Y. Cao, Regulating the solvation sheath of zinc ions by supramolecular coordination chemistry toward ultrastable zinc anodes, SmartMat (2023) e1216.

[46] Y. Zhang, G. Wan, N.H.C. Lewis, J. Mars, S.E. Bone, H.-G. Steinrück, M.R. Lukatskaya, N.J. Weadock, M. Bajdich, O. Borodin, Water or anion? Uncovering the Zn2+ solvation environment in mixed Zn (TFSI) 2 and LiTFSI water-in-salt electrolytes, ACS Energy Letters 6(10) (2021) 3458-3463.

[47] P.S. Salmon, M.C. Bellissent-Funel, G.J. Herdman, The dynamics of aqueous Zn2+ solutions: a study using incoherent quasi-elastic neutron scattering, Journal of Physics: Condensed Matter 2(18) (1990) 4297.

[48] B.F. Abrahams, M. Moylan, S.D. Orchard, R. Robson, Zinc saccharate: a robust, 3D coordination network with two types of isolated, parallel channels, one hydrophilic and the other hydrophobic, Angewandte Chemie International Edition 42(16) (2003) 1848-1851.

[49] I. Labadi, L. Parkanyi, G. Kenessey, G. Liptay, Thermal stability and crystal structure of bis (1, 2 ethanediol) zinc sulfate, Journal of crystallographic and spectroscopic research 23 (1993) 333-338.

[50] V. Verma, R.M. Chan, L. Jia Yang, S. Kumar, S. Sattayaporn, R. Chua, Y. Cai, P. Kidkhunthod, W. Manalastas Jr, M. Srinivasan, Chelating ligands as electrolyte solvent for rechargeable zinc-ion batteries, Chemistry of Materials 33(4) (2021) 1330-1340.

[51] E.L. Lindh, C. Terenzi, L. Salmén, I. Furo, Water in cellulose: evidence and identification of immobile and mobile adsorbed phases by 2 H MAS NMR, Physical Chemistry Chemical Physics 19(6) (2017) 4360-4369.

[52] J.C. Wu, J.-P. Piquemal, R. Chaudret, P. Reinhardt, P. Ren, Polarizable molecular dynamics simulation of Zn (II) in water using the AMOEBA force field, Journal of chemical theory and computation 6(7) (2010) 2059-2070.

[53] A. Malinowski, M. Śmiechowski, Solvent Exchange around Aqueous Zn (II) from Ab Initio Molecular Dynamics Simulations, Liquids 2(3) (2022) 243-257.

[54] H. Zhang, X. Gan, Z. Song, J. Zhou, Amphoteric Cellulose-Based Double-Network Hydrogel Electrolyte Toward Ultra-Stable Zn Anode, Angewandte Chemie 135(13) (2023) e202217833.

[55] K. Chen, J. Huang, J. Yuan, S. Qin, P. Huang, C. Wan, Y. You, Y. Guo, Q. Xu, H. Xie, Molecularly engineered cellulose hydrogel electrolyte for highly stable zinc ion hybrid capacitors, Energy Storage Materials 63 (2023) 102963.

[56] Y. Hao, D. Feng, L. Hou, T. Li, Y. Jiao, P. Wu, Gel electrolyte constructing Zn (002) deposition crystal plane toward highly stable Zn anode, Advanced Science 9(7) (2022) 2104832.